

4D-STEM Mapping of Nanocrystal Reaction Dynamics and Heterogeneity in a Graphene Liquid Cell

Chang Liu, Oliver Lin, Saran Pidaparthi, Haoyang Ni, Zhiheng Lyu, Jian-Min Zuo, and Qian Chen*



Cite This: <https://doi.org/10.1021/acs.nanolett.3c05015>



Read Online

ACCESS |



Metrics & More



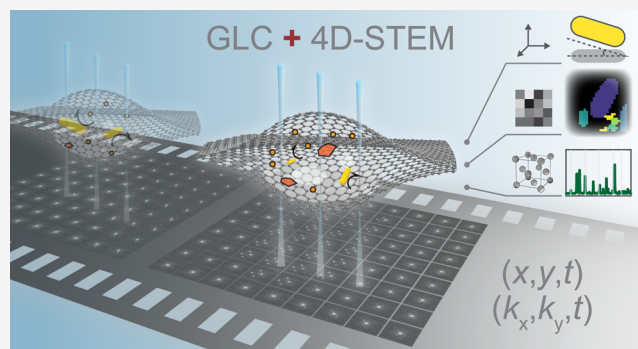
Article Recommendations



Supporting Information

ABSTRACT: Chemical reaction kinetics at the nanoscale are intertwined with heterogeneity in structure and composition. However, mapping such heterogeneity in a liquid environment is extremely challenging. Here we integrate graphene liquid cell (GLC) transmission electron microscopy and four-dimensional scanning transmission electron microscopy to image the etching dynamics of gold nanorods in the reaction media. Critical to our experiment is the small liquid thickness in a GLC that allows the collection of high-quality electron diffraction patterns at low dose conditions. Machine learning-based data-mining of the diffraction patterns maps the three-dimensional nanocrystal orientation, groups spatial domains of various species in the GLC, and identifies newly generated nanocrystallites during reaction, offering a comprehensive understanding on the reaction mechanism inside a nanoenvironment. This work opens opportunities in probing the interplay of structural properties such as phase and strain with solution-phase reaction dynamics, which is important for applications in catalysis, energy storage, and self-assembly.

KEYWORDS: Four-dimensional scanning transmission electron microscopy, graphene liquid cell electron microscopy, nanocrystal etching dynamics, nanostructural heterogeneity



Chemical reaction kinetics and the associated nanoscale spatial heterogeneity in the reactants and reaction environment such as reactant composition, solution structure, and temperature are interdependent in various systems.^{1,2} For example, local variations in monomer concentrations can impact interfacial polymerization kinetics in the synthesis of polyamide membranes, leading to the formation of nanoscale Turing patterns.³ A structurally heterogeneous solid–electrolyte interphase can impede or promote ion diffusion in rechargeable ion batteries.⁴ For nanocrystals, they have diverse applications in bioimaging, photoemission, energy storage, and mechanical and optical metamaterials.⁵ The associated reactions such as growth and etching can all be affected by nanostructural heterogeneity.⁶ The heterogeneity can be of nanocrystals, such as spatial differences in phase, phase orientation, and strain, which determine the local reactivities of nanocrystals.^{4,7–11} The heterogeneity can also occur in the reaction media of the nanocrystals, such as solvated ligands and ion clusters, which change local reaction kinetics.^{12–15} While recent advancements of liquid-phase transmission electron microscopy (TEM) have enabled direct observations of the reaction kinetics of nanocrystals in liquids at the unparalleled nanometer (nm) resolution, the involved nanostructural features of the nanocrystals and liquid environment have not been simultaneously studied. TEM imaging only resolves the size, shape, and position of the samples. Without indexing the

three-dimensional (3D) nanocrystal orientation, the analysis of nanocrystal reaction trajectories has been restricted by two-dimensional (2D) TEM projections and by assuming the absence of out-of-plane nanocrystal rotation. Without mapping the phases in the liquid reaction media, it is difficult to consider their impact on reaction kinetics where side reactions or even phase transitions can occur, which is complex, heterogeneous, and temporally evolving.^{2,16}

Complementarily, the recently emergent four-dimensional scanning transmission electron microscopy (4D-STEM) utilizes a nm-sized probe to raster scan a region of interest (ROI) and to collect electron diffraction patterns (DPs), from which the crystal identity, crystal orientation, extent of disorder, and strain of the ROI can be mapped at nm resolution.¹⁷ However, 4D-STEM has only been scantily demonstrated in a liquid TEM chamber *without temporal dynamics*. Because the quality of DPs of a nm-by-nm sample area decays fast in the presence of thick liquid along the beam

Received: December 20, 2023

Revised: March 14, 2024

Accepted: March 15, 2024

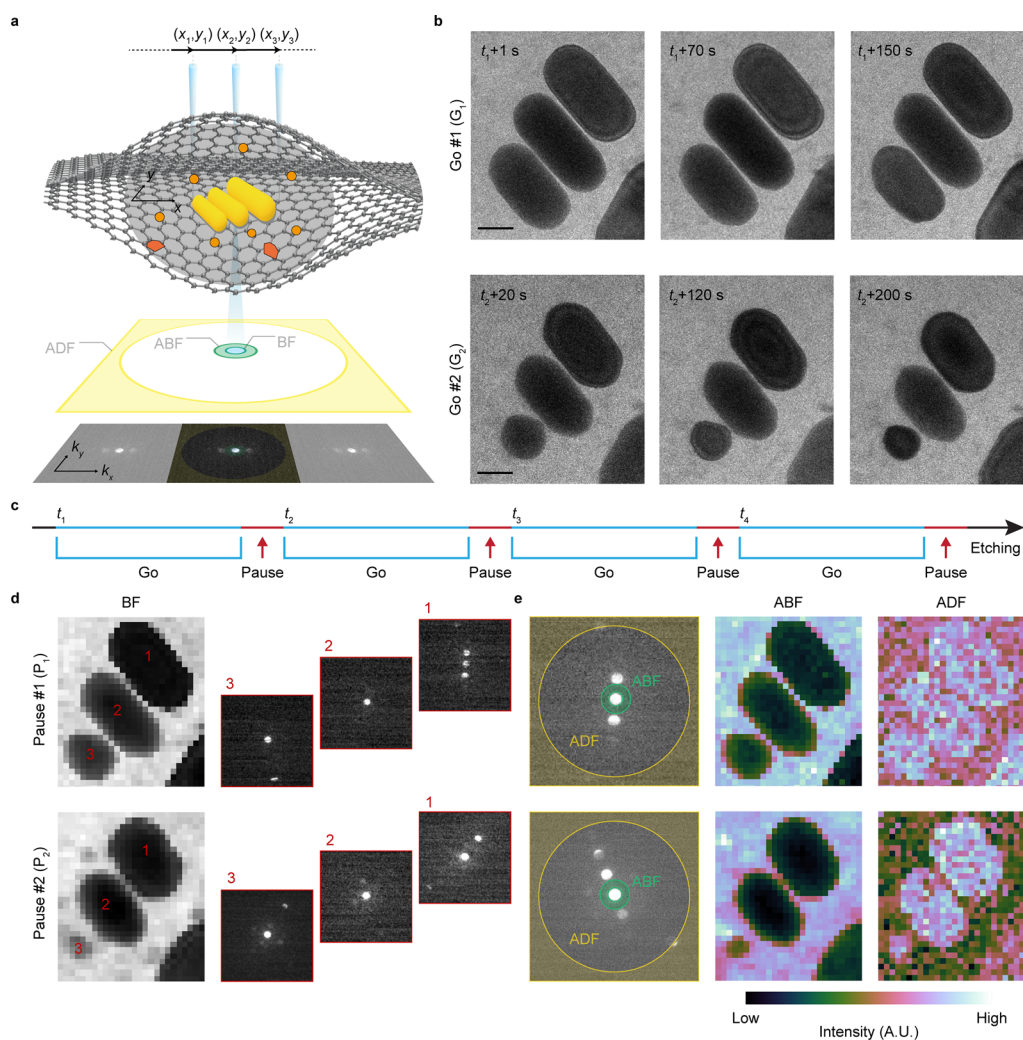


Figure 1. Experimental workflow of our “4D-STEM in a GLC” method and representative 4D-STEM dataset during the etching reaction of GNRs. (a) The schematic of our 4D-STEM in a GLC experiment and the different virtual detectors. (b) Time-lapse liquid-phase TEM images showing the etching process of three GNRs in two sequential “Go” sessions (G_1 and G_2). Scale bars: 50 nm. Dose rate: $273.0 \text{ e}^- \text{ \AA}^{-2} \text{ s}^{-1}$. (c) Schematic of “pause-and-go” cycles during the etching of GNRs. (d) Reconstructed BF images (left) and averaged DPs of GNRs at two “Pause” sessions (P_1 and P_2). The time taken for 4D-STEM DP collection is 19 min for Pause 1 and 14 min for Pause 2. (e) Reconstructed ABF (middle) and ADF (right) images from different DP areas colored (left). Pixel size in the virtual images in (d) and (e): $5 \text{ nm} \times 5 \text{ nm}$.

path, previous studies used either strong beam illumination or electric biasing to induce bubble formation and liquid thinning in a SiN_x chamber.^{18,19} These studies have difficulty in controlling the remanent liquid amount and, more importantly, altered the liquid. Recent work by Xie and Wang et al. used a carbon-film liquid sandwich, which is thinner than a SiN_x liquid chamber, to achieve 4D-STEM mapping of the nanostructures of electrolytes;⁸ the electrolytes maintained a solvated but static structure, without diffusional or reactional dynamics.

Here we achieve the first correlated imaging of reaction dynamics and nanostructural heterogeneity of nanocrystals by 4D-STEM in a graphene liquid cell (GLC), which reveals the etching trajectories, the 3D orientation dynamics of the nanocrystals, and temporally evolving heterogeneity in the GLC (Figure 1a). GLC has been known for its thinnest possible membranes,^{20,21} utilizing which we collect high-quality 4D-STEM datasets for liquid samples at nm resolution. Using the etching reaction of gold nanorods (GNRs) as the model system, we perform 4D-STEM within micrometer-sized

ROIs, including GNRs and the surrounding etching solution at different reaction stages. Our customized machine learning (ML)-based data-mining of the 4D-STEM datasets allows us to (i) reconstruct virtual bright field (BF), annular bright field (ABF), and annular dark-field (ADF) images of the ROI that are consistent with real-space liquid-phase TEM images; (ii) perform DP clustering analysis to recognize all species within the GLC, including GNRs, nanocrystalline and amorphous species in the liquid regions; (iii) index the 3D orientation of GNRs and identify the nanocrystalline species that are otherwise hard to distinguish in TEM mode; (iv) correlate (i)–(iii) in the temporal domain with the etching of GNRs continuously captured in TEM to gain insights in the etching kinetics. Our “4D-STEM in a GLC” method integrates nm-resolution mapping of real-space etching kinetics and reciprocal-space crystallographic information, opening opportunities in studying solution-phase reactions where nanostructural heterogeneity is critical, such as heterostructured nanocrystals that we demonstrate here using multitwinned icosahedral nanoparticles (MTNPs), strain-dependent nano-

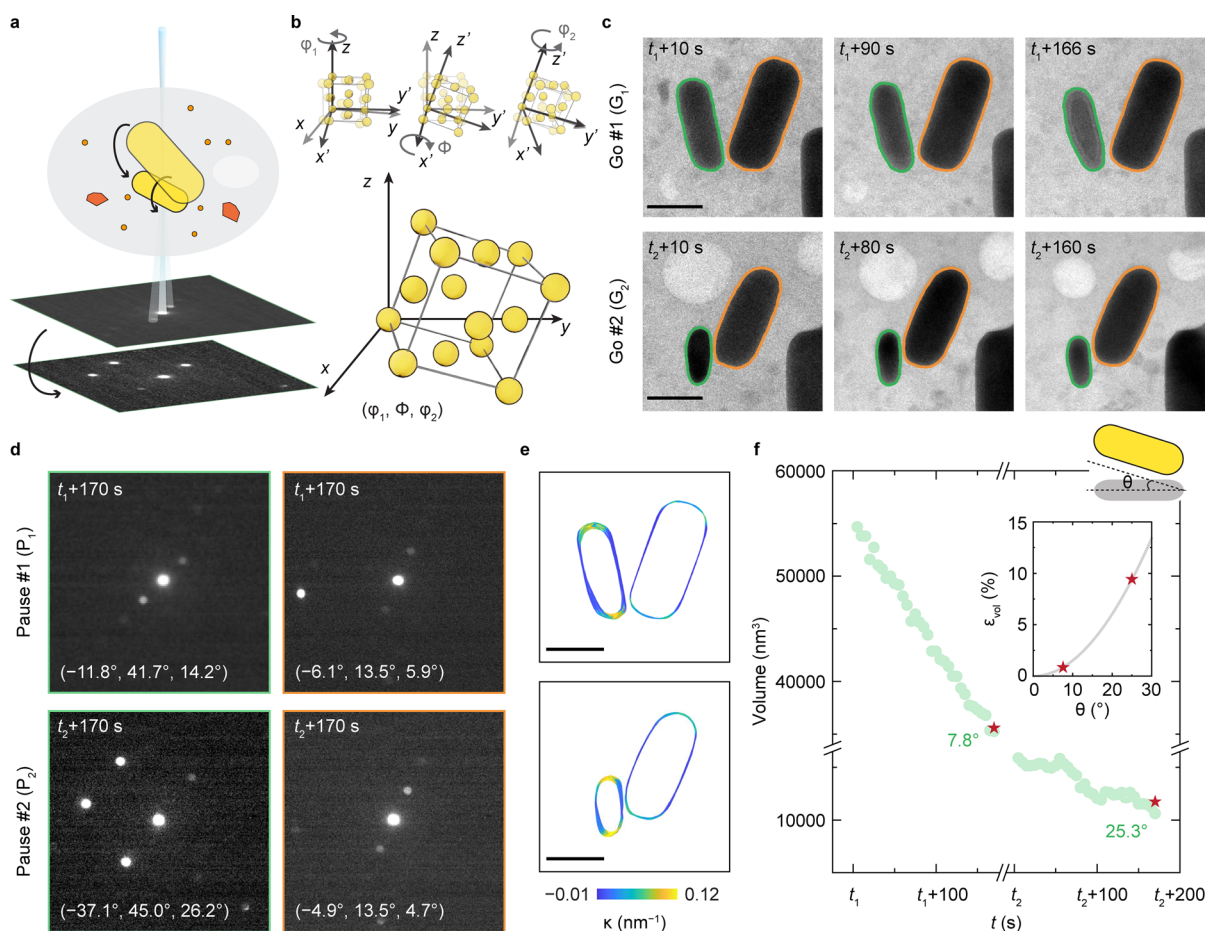


Figure 2. 3D rotational dynamics of GNRs during etching. (a) Schematic of 3D rotation of GNRs in GLC during etching with their corresponding averaged DPs captured using 4D-STEM. (b) Definition of Bunge angle in a face-centered cubic (*fcc*) unit cell. The rotation follows the sequence of $(\varphi_1, \Phi, \varphi_2)$ around the z, x', z' axis, respectively. (c) Time-lapse liquid-phase TEM images with the contours of the GNRs tracked showing the etching process in two sequential sessions (G_1 and G_2). Dose rate: $334.4 \text{ e}^- \text{ \AA}^{-2} \text{ s}^{-1}$. (d) Averaged DPs of two GNRs at Pause 1 (P_1 and P_2) showing the orientations of the Au crystals. The time taken for 4D-STEM DP collection is 45 min for Pause 1 and 11 min for Pause 2. The Bunge angles for each GNR at each stage are marked. (e) GNR projection contours colored to their local surface curvatures during etching showing the projected morphological change. (f) Volume trajectories of the small GNR. The highlighted stars are corrected values based on the marked tilting angle θ derived from Bunge angles $(\varphi_1, \Phi, \varphi_2)$ in (d). Inset: Corrected volumetric error ϵ_{vol} as a function of tilting angle θ . Scale bars: 50 nm.

catalyst reactivity, and rotational dynamics of nanocrystals in bioimaging and self-assembly.

We first use single-crystalline GNRs synthesized following the literature and mix them with aqueous FeCl_3 and Tris-HCl solution (Figures 1a and S1, Movie S1), sealed in a GLC.²² The etching solution induces etching of GNRs at dose rates of $273.0\text{--}334.4 \text{ e}^- \text{ \AA}^{-2} \text{ s}^{-1}$ in the TEM mode. At these dose rates, radiolysis products such as OH^\bullet can have high enough concentration to couple with oxidative Fe^{3+} and etch GNRs as captured by liquid-phase TEM (Figure 1b).¹³ Meanwhile, the FeCl_3 concentration is low enough to present no etching in the TEM mode at dose rates lower than $5 \text{ e}^- \text{ \AA}^{-2} \text{ s}^{-1}$.^{23,24} Accordingly, we developed multiple “Pause-and-Go” cycles of alternating TEM imaging and 4D-STEM collection (Figures 1c and S2). During “Go” sessions, liquid-phase TEM imaging triggers the reaction at the high dose rate in real-time. At “Pause” sessions, to map nanostructural heterogeneity, 4D-STEM is performed based on Scanning Electron Nanodiffraction (SEND) previously described (Supporting Information).²⁵

For the 4D-STEM datasets collected at two etching stages (Figure 1d, e), different virtual detectors can be selected to

access various contrast mechanisms and to recognize different components in the sample (Figure 1a). For example, in Figure 1d, BF images are reconstructed based on the transmitted beam in DPs (blue area, Figure 1a), with a bright liquid region and dark GNR regions due to the fact that the short-range ordered or amorphous structure scatters near the transmitted beam where no Bragg spots from the crystalline GNRs are present. Virtual BF thus creates contrast similar to bright field TEM imaging; the morphologies of GNRs match with those in liquid-phase TEM movies, validating the quality of DPs for further analysis. The DPs of individual GNRs (Figure 1d) show distinct diffraction spots, suggesting different crystalline orientations. Next, Figure 1e shows ABF images reconstructed from the detector area between the transmitted beam and the first order Bragg reflection from GNR lattices (green area, Figure 1a, e). The ABF images highlight the weakly scattering and short-ranged structures such as the liquid in the GLC.²⁶ Then the ADF images in Figure 1e use the high angle areas of the DPs (yellow areas, Figure 1a, e), which present the crystalline (dominantly GNR) regions as high intensity features. Altogether, different virtual detectors for the 4D-

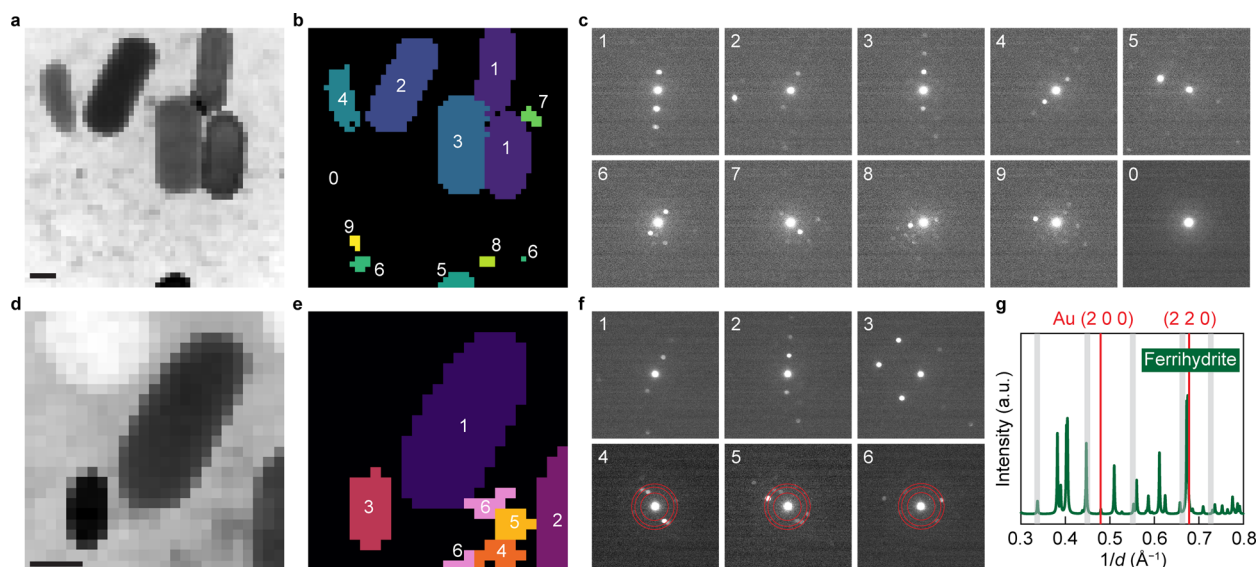


Figure 3. Crystalline information mapping and identification. (a, d) Reconstructed BF images of the GLC after etching at P₁ and P₂. (b, e) Grouping results showing different components in the GLC, including both GNRs and different ferric oxyhydroxide nanocrystals. Crystals with different orientations are colored differently. (c, f) Averaged DPs of each group in (b) and (e) showing clear identification of the varying components in liquid. The gold (200), (220), and (311) are highlighted as rings for calibration. (g) Diffraction profiles of the ferrihydrite. The positions of experimental diffraction spots are marked with gray stripes overlapping the peak positions. The width of the stripes corresponds to 1 pixel in DP images. Scale bars: 50 nm.

STEM datasets distinguish low *z*-contrast species and their morphologies based on the phase information.

Further quantitative analysis of the DPs of GNRs maps crystal orientations, which enables indexing of the 3D orientations and out-of-plane rotations of GNRs (Figure 2a–b, Movie S2) as they undergo etching in the GLC, which is not accessible to liquid-phase TEM imaging. Specifically, two GNRs are shown as examples, which undergo etching during successive “Go” sessions as their projected contours change (Figure 2c). 4D-STEM datasets are collected after each etching stage, and then the DPs belonging to the two GNRs are each identified and averaged to improve indexing reliability (Figure 2d). These DPs are fitted to a simulated DP database for the most probable crystalline orientation (Figure S3, Supporting Information), represented by the Bunge angles following the sequence $(\varphi_1, \Phi, \varphi_2)$ (Figure 2b). Correspondingly, the 3D orientations of GNRs are derived as the out-of-plane tilting angle, θ (Figure 2f).

Unlike previous GLC studies where etching dynamics were studied by assuming all nanoparticles have no out-of-plane rotations, we find that θ changes as etching proceeds.^{27,28} The small GNR rotates significantly out-of-plane from $\theta = 7.8^\circ$ to 25.3° , while the big GNR rotates much less, from $\theta = 1.4^\circ$ to 1.1° (Figure 2d, Supporting Information). We correct the 2D projected area of the GNRs (stars in Figure 2f) by a factor of ε_{vol} based on θ , to derive the 3D volumetric changes. The correction (ε_{vol}), although about 0.9% for the big GNR, is as high as 9.6% for the small GNR, significant to consider for etching rates (Figure 2f, inset; Figure S4, Supporting Information). Note that our 4D-STEM-based measurement of the 3D nanoparticle orientation is different from electron tomography; 4D-STEM does not require the collection of tilt series or extended beam illumination, thereby maximally maintaining the reaction environment to allow monitoring of temporal changes. Different GNRs rotate differently in 3D,

demonstrating the complexity of the etching kinetics and the necessity of real-space imaging.

During the etching process, species other than GNRs within the ROI can be captured by 4D-STEM. As shown in Figure 3a–f, we develop a generalizable workflow to calculate the cross-correlation coefficients of all DPs and classify them into groups by the *k*-means method (Figure S5 and Supporting Information) without knowing *a priori* the existing species. In the example of the ROI in Figure 3a, different groups of DPs are clustered and labeled in real-space (Figure 3b). In addition to the expected groups from GNRs (1–5 in Figure 3b), multiple other groups are distinct from the scattering background and appear as small domains (6–9 in Figure 3b). These small domains can hardly be differentiated in the virtual BF image in Figure 3a. Similar observations are made at the “Pause 2” stage in a zoomed-in view of the same ROI (Figure 3d–e). The DPs of the non-GNR groups suggest nucleation of nanocrystals in the vicinity of the GNRs.

The DPs of the small non-GNR crystalline domains are used as powder diffraction patterns to specify their chemical composition and structure. The diffraction disc pairs in groups 6–8 and group 9 in Figure 3c measure to $(0.338 \pm 0.0066) \text{ \AA}^{-1}$ and $(0.551 \pm 0.0066) \text{ \AA}^{-1}$ respectively, which do not match with the gold lattice *d*-spacing. The closest *d*-spacings of the gold (111), (200), and (220) planes (overlaid in Figure 3f) do not match with the diffraction spots either, suggesting that new crystalline species other than gold have been formed in the GLC. At the nanoscale, Navrotsky et al. predicted the thermodynamics and reactivity of iron oxide in various phases and hydration states based upon their sizes.²⁹ Upon first hydration ($\text{Fe}_2\text{O}_3 + \text{H}_2\text{O} \rightarrow 2\text{FeOOH}$), iron oxyhydroxides, nominally FeOOH, have four known phases while there exists subsequent hydration to form ferrihydrite ($\text{FeOOH} + \text{H}_2\text{O} \rightarrow \text{Fe}(\text{OH})_3$). Their study showed that ferrihydrite is the most thermodynamically competitive among all of the species at a size of ~ 60 nm or smaller. Here by measuring the *d*-spacing of

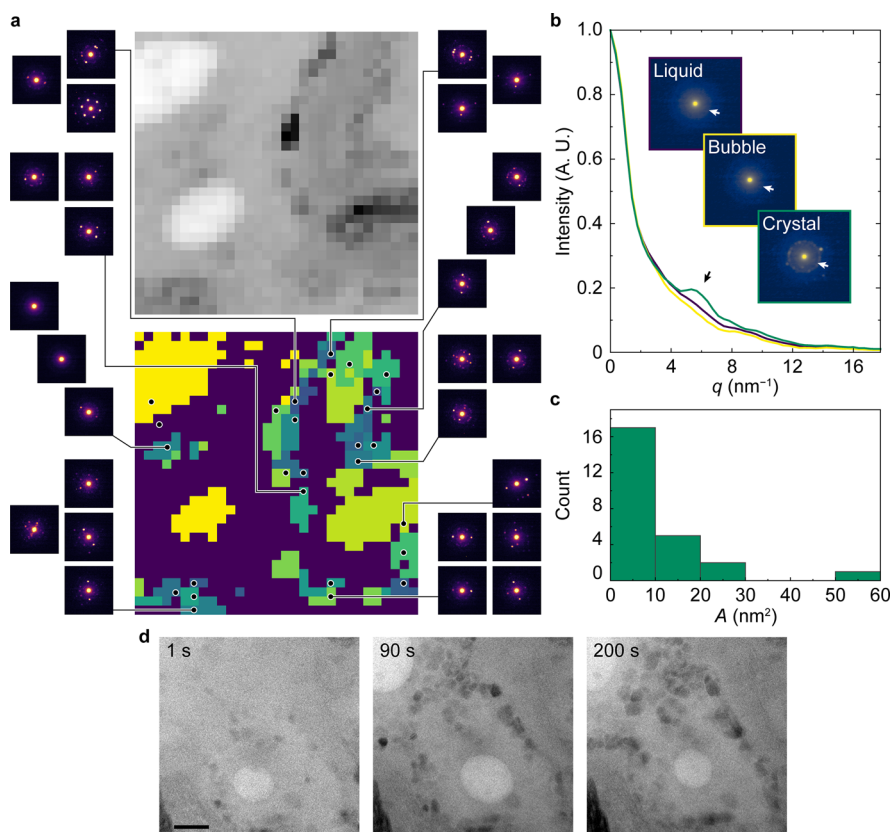


Figure 4. Heterogeneity mapping in the liquid environment of a GLC. (a) Heterogeneity mapping of the GLC after TEM imaging at the dose rate of $334.4 \text{ e}^- \text{ \AA}^{-2} \text{ s}^{-1}$. Liquid (purple), bubbles (yellow), and nanocrystals (green) are identified clearly using the grouping method. Time taken to collect DPs: 30 min. (b) Radial intensity profiles of averaged DPs of liquid, bubble, and crystal regions. To highlight features, all the data are normalized. Although both DPs of liquid and bubble show no diffraction spots and look similar, the liquid DP has a more diffusive inner disc due to the inelastic scattering of water, resulting in a higher intensity at pointed q , while the bubble DP shows a sharper inner disc. Inset: Averaged DPs of liquid, bubble, and crystal regions. (c) Histogram of the size of different crystalline groups in (a) showing the heterogeneous environment in the GLC. (d) Time-lapse liquid-phase TEM images showing the evolution of the bubbles together with the nanocrystals. Scale bars: 50 nm.

all the diffraction discs available ($0.338, 0.449, 0.551, 0.662,$ and 0.727 \AA^{-1} , gray in Figure 3g) against the powder patterns of all the chemicals with known crystal structures in the series of hydration reactions, we find that ferrihydrite indeed has the most peaks matched (Figures 3g and S6). In addition, Michel et al. reported that the prevalent nanocrystalline ($<10 \text{ nm}$) form of ferrihydrite in a broad range of applications exhibits slightly different crystal structures at domain sizes of 2, 3, and 6 nm (not in GLC).³⁰ Similarly, our grouping results show that most of the nanocrystalline domain sizes are no larger than 10 nm. While previous GLC studies have also observed nanocrystallites when their size was sufficiently large ($>10 \text{ nm}$) to image under TEM, the compositions of the crystallites were assigned as FeOOH or $\text{Fe}(\text{OH})_3(\text{H}_2\text{O})_{0.25}$, based on real-space imaging of lattice fringes under a strong electron beam.^{12,31} 4D-STEM instead scans across an ROI and locates the nanocrystallites at a more nascent stage of a small size with a low electron dose rate, because DPs are sensitive to local periodic structures and can measure multiple d -spacings of randomly oriented nanocrystallites for precise identification of phases.

To fully exploit 4D-STEM to map and detect species that are otherwise “invisible” in the TEM imaging, we map the etching solution in the GLC without GNRs, which shows an obvious heterogeneity that was discussed in previous literature reports (Movie S3).^{27,28} As shown in Figure 4a, virtual BF

images and grouped DPs of the liquid pocket suggest immediate spatial heterogeneity of the reaction environment, i.e., bubbles, liquids, and nanocrystallites. The average DPs of each group are shown in Figure 4b. The DPs of nanocrystallites exhibit distinctive and sharp spots while those of the liquid and bubble domains have diffuse scattering around the transmitted beam. Between liquid and bubbles, although both show amorphous rings, the liquid DP has a more diffusive inner disc due to the inelastic scattering of water, resulting in a higher intensity at pointed q , while the bubble DP shows a sharper inner disc (Figure 4b). Our grouping separates the two amorphous species apart. During 4D-STEM mapping, the morphology of nanobubbles and nanocrystals remains intact, suggesting that the electron beam effect is generally minimized at this “Pause” stage. The radiolysis of the aqueous solution at high dose rate generates H_2 , which further nucleates into bubbles.^{32–34} The DPs of the nanocrystallites match with those of ferrihydrite oriented at the zone axis (001), which can be possibly attributed to pH induced precipitation of Fe^{3+} ions, exhibiting spatial domains of various sizes. 4D-STEM and analysis of DPs uniquely allow us to spatially map different chemical identities such as liquid, bubble, gold nanocrystals, and ferrihydrites (even those with sizes below 60 nm^2 , Figure 4c), which are hard to identify all at once using traditional TEM.

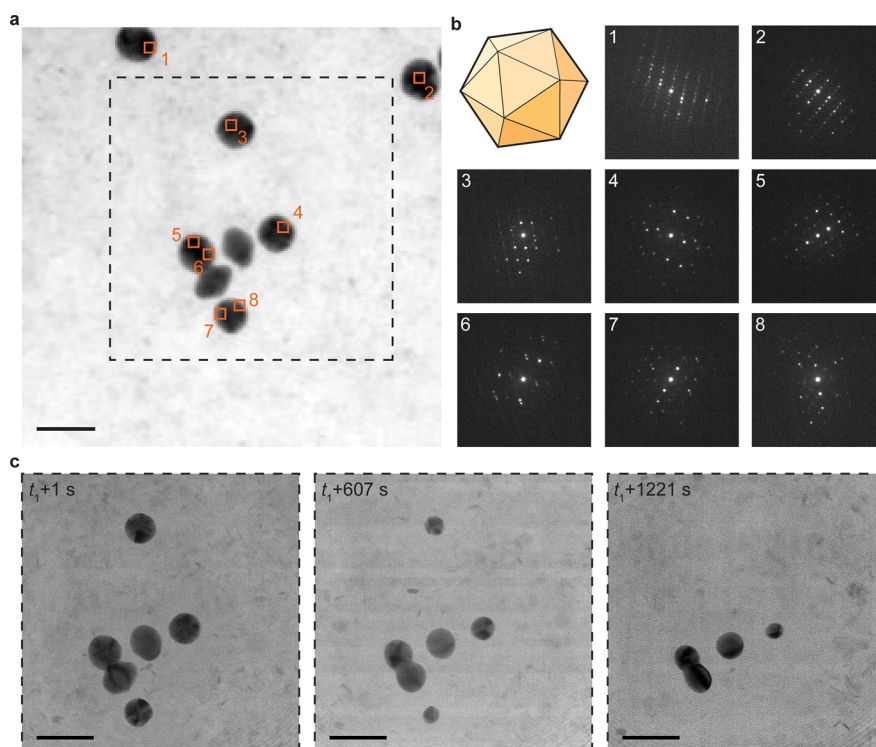


Figure 5. 4D-STEM-in-a-GLC experiment with gold MTNPs. (a) Virtual BF image of MTNPs in GLC. (b) MTNPs with twin boundaries and representative DPs of the regions highlighted in (a). Time taken for 4D-STEM DP collection: 120 s. (c) Time-lapse liquid-phase TEM images showing the etching of MTNPs in a GLC. Scale bars: 50 nm.

The spatial and chemical heterogeneities of the etching solution in GLCs are common and evolve over time and are found to correlate with local changes in etching kinetics. For example, it was reported that beam-generated gas bubbles can significantly accelerate the oxidative etching of gold NPs.³² Indeed, the small GNR in Figures 2c and S8, with a nanobubble close to its lower left bottom, shows faster etching than the big GNR, leaving a dip at the bottom left tip (purple arrows in Figure S8b). Meanwhile, the formation of ferrihydrite nanocrystallites suggests local consumption of Fe^{3+} ions in addition to those reacted during etching, which leads to differences in the local etching rate of GNRs (examples in Figure S8b) and symmetry-breaking in the GNR shape. Such a heterogeneous environment can originate from stochastic nucleation of crystallites and bubbles during reactions, the limited diffusion of ions within a confined GLC pocket, and the variation of the surface chemistry of graphene. Our observation suggests that in future studies to use GLC as nanoreactors, such heterogeneity needs to be considered in explaining reaction kinetics.

In summary, we show the GLC-based 4D-STEM studies of nanocrystal reaction kinetics and structural heterogeneity, showing the resulting capability of quantitative analysis of temporally evolving structure and phases in a liquid environment at the nanoscale. For GNRs sandwiched in an etching solution, we find out-of-plane rotational motions, which are important to consider for understanding the etching kinetics in 3D. Significant heterogeneity in the GLC is detected from DPs collected at nm step size, allowing us to track and identify the emergence of phases that are otherwise hard to visualize in TEM alone.

The experimental imaging and analysis platform can be applied to other systems such as MTNPs to study their

structural evolution during chemical reactions (Figure 5, Methods, Supporting Information). Figure 5a–b shows that 4D-STEM maps distinctive DPs which are due to either the existence of different crystal orientations within one MTNP or the superpositions of all the DPs from the domains along the beam path. These MTNPs can merely be recognized as circular projections in TEM alone where the multicrystallinity is lost. It is possible to decouple the superpositioned DPs for further analysis on such complicated structures. Since GLC can be held by double-tilt holders, one can also use single crystals to understand the influence of excitation error on the intensities of forbidden reflections in the GLCs. Similar to GNRs, MTNP etching can be initiated at dose rates of $35.6\text{--}152.6\text{ e}^- \text{ \AA}^{-2} \text{ s}^{-1}$ under TEM over extended observation time (~ 20 min) with an accumulated dose of $144,000\text{ e}^- \text{ \AA}^{-2}$, without observing drying of GLCs while maintaining continuous etching of the nanoparticles (Figure S9, Table S2). In 4D-STEM, with a fixed dose rate of $1.5 \times 10^5\text{ e}^- \text{ \AA}^{-2} \text{ s}^{-1}$ and ~ 60 s duration for each 4D-STEM scan, more than 15 rounds of 4D-STEM DP collections can be performed during multiple “Pause” sessions while the etching of MTNPs can proceed in the “Go” sessions (Figure 5c, Table S1). Note that for the “Pause” sessions to collect 4D-STEM DPs, we find that an accumulated dose of $7.5 \times 10^7\text{ e}^- \text{ \AA}^{-2}$ (Figure S10 and Table S3) can start to initiate the etching of NPs by the scanning probe. The “Pause” sessions can be further shortened with advanced instrumentation such as new detectors and data transfer schemes. For example, to our estimation, a pixelated direction electron detector with a speed of 1,000 frames per second, such as an Electron Microscope Pixel Array Detector (EMPAD), can have a 60- to 100-fold decrease in the acquisition time at a similar ROI size at lower dose, pushing the acquisition time from ~ 30 min to tens of seconds.³⁵ As to pushing for the atomic

resolution in 4D-STEM, previous work has shown that advanced nanofabrication of 2D materials has made GLCs that allow HAADF-STEM imaging of single metallic atoms.³⁶ We foresee that *ptychography* reconstruction of atomic images in 4D-STEM is feasible in GLC, especially with recent advances in compressive sensing algorithms to reduce the dose needed³⁷ and the development of the next generation of direct electron detectors, such as EMPAD-G2 and Dectris detectors. As such, we see that our 4D-STEM-in-a-GLC method can provide a comprehensive mapping of the heterogeneity in reaction kinetics by capturing structural complexities of multiphased nanocrystals, spatial distribution of strain, which can relate to catalytic activity, and amorphous species such as ligand structures on nanoscale surfaces.

■ ASSOCIATED CONTENT

SI Supporting Information

The Supporting Information is available free of charge at <https://pubs.acs.org/doi/10.1021/acs.nanolett.3c05015>.

Experimental materials and methods; analysis (indexing of DPs, calculations and corrections of GNR volume, grouping of DPs, chemical identification) (PDF)

Movie S1. "Pause-and-Go" etching of GNRs with reconstructed images from 4D-STEM (MP4)

Movie S2. "Pause-and-Go" etching of GNRs with grouping results from 4D-STEM (MP4)

Movie S3. Heterogeneity mapped in GLC (MP4)

■ AUTHOR INFORMATION

Corresponding Author

Qian Chen – Department of Materials Science and Engineering, Department of Chemistry, Materials Research Laboratory, and Beckman Institute for Advanced Science and Technology, University of Illinois, Urbana, Illinois 61801, United States; orcid.org/0000-0002-1968-441X; Email: qchen20@illinois.edu

Authors

Chang Liu – Department of Materials Science and Engineering, University of Illinois, Urbana, Illinois 61801, United States; orcid.org/0000-0001-8091-7940

Oliver Lin – Department of Chemistry, University of Illinois, Urbana, Illinois 61801, United States

Saran Pidaparthi – Department of Materials Science and Engineering, University of Illinois, Urbana, Illinois 61801, United States; orcid.org/0000-0002-0783-3094

Haoyang Ni – Department of Materials Science and Engineering, University of Illinois, Urbana, Illinois 61801, United States

Zhiheng Lyu – Department of Materials Science and Engineering, University of Illinois, Urbana, Illinois 61801, United States; orcid.org/0000-0002-1343-4057

Jian-Min Zuo – Department of Materials Science and Engineering and Materials Research Laboratory, University of Illinois, Urbana, Illinois 61801, United States; orcid.org/0000-0002-5151-3370

Complete contact information is available at: <https://pubs.acs.org/doi/10.1021/acs.nanolett.3c05015>

Notes

The authors declare no competing financial interest.

■ ACKNOWLEDGMENTS

This material is based upon work supported by the U.S. Department of Energy, Office of Science, Office of Basic Energy Sciences, under Award Number DE-SC0024064. Experiments were carried out in part in the Materials Research Laboratory Central Research Facilities, University of Illinois.

■ REFERENCES

- (1) Chee, S. W.; Tan, S. F.; Baraissov, Z.; Bosman, M.; Mirsaidov, U. Direct Observation of the Nanoscale Kirkendall Effect during Galvanic Replacement Reactions. *Nat. Commun.* **2017**, *8*, 1224.
- (2) Loh, N. D.; Sen, S.; Bosman, M.; Tan, S. F.; Zhong, J.; Nijhuis, C. A.; Král, P.; Matsudaira, P.; Mirsaidov, U. Multistep Nucleation of Nanocrystals in Aqueous Solution. *Nat. Chem.* **2017**, *9*, 77–82.
- (3) An, H.; Smith, J. W.; Ji, B.; Cotty, S.; Zhou, S.; Yao, L.; Kalutanirige, F. C.; Chen, W.; Ou, Z.; Su, X.; Feng, J.; Chen, Q. Mechanism and Performance Relevance of Nanomorphogenesis in Polyamide Films Revealed by Quantitative 3D Imaging and Machine Learning. *Sci. Adv.* **2022**, *8*, No. eakb1888.
- (4) Chen, W.; Zhan, X.; Yuan, R.; Pidaparthi, S.; Yong, A. X. B.; An, H.; Tang, Z.; Yin, K.; Patra, A.; Jeong, H.; Zhang, C.; Ta, K.; Riedel, Z. W.; Stephens, R. M.; Shoemaker, D. P.; Yang, H.; Gewirth, A. A.; Braun, P. V.; Ertekin, E.; Zuo, J. M.; Chen, Q. Formation and Impact of Nanoscopic Oriented Phase Domains in Electrochemical Crystalline Electrodes. *Nat. Mater.* **2023**, *22*, 92–99.
- (5) Boles, M. A.; Engel, M.; Talapin, D. V. Self-Assembly of Colloidal Nanocrystals: From Intricate Structures to Functional Materials. *Chem. Rev.* **2016**, *116*, 11220–11289.
- (6) Lyu, Z.; Yao, L.; Chen, W.; Kalutanirige, F. C.; Chen, Q. Electron Microscopy Studies of Soft Nanomaterials. *Chem. Rev.* **2023**, *123*, 4051–4145.
- (7) Hutzler, A.; Schmutzler, T.; Jank, M. P. M.; Branscheid, R.; Unruh, T.; Spiecker, E.; Frey, L. Unravelling the Mechanisms of Gold-Silver Core-Shell Nanostructure Formation by in Situ TEM Using an Advanced Liquid Cell Design. *Nano Lett.* **2018**, *18*, 7222–7229.
- (8) Xie, Y.; Wang, J.; Savitzky, B. H.; Chen, Z.; Wang, Y.; Betzler, S.; Bustillo, K.; Persson, K.; Cui, Y.; Wang, L.-W.; Ophus, C.; Ercius, P.; Zheng, H. Spatially Resolved Structural Order in Low-Temperature Liquid Electrolyte. *Sci. Adv.* **2023**, *9*, No. eadc9721.
- (9) Shi, F.; Gao, W.; Shan, H.; Li, F.; Xiong, Y.; Peng, J.; Xiang, Q.; Chen, W.; Tao, P.; Song, C.; Shang, W.; Deng, T.; Zhu, H.; Zhang, H.; Yang, D.; Pan, X.; Wu, J. Strain-Induced Corrosion Kinetics at Nanoscale Are Revealed in Liquid: Enabling Control of Corrosion Dynamics of Electrocatalysis. *Chem.* **2020**, *6*, 2257–2271.
- (10) Liu, L.; Sassi, M.; Zhang, X.; Nakouzi, E.; Kovarik, L.; Xue, S.; Jin, B.; Rosso, K. M.; De Yoreo, J. J. Understanding the Mechanisms of Anisotropic Dissolution in Metal Oxides by Applying Radiolysis Simulations to Liquid-Phase TEM. *Proc. Natl. Acad. Sci. U S A* **2023**, *120*, No. e2101243120.
- (11) Leonardi, A.; Engel, M. Particle Shape Control via Etching of Core@Shell Nanocrystals. *ACS Nano* **2018**, *12*, 9186–9195.
- (12) Hauwiller, M. R.; Ondry, J. C.; Chan, C. M.; Khandekar, P.; Yu, J.; Alivisatos, A. P. Gold Nanocrystal Etching as a Means of Probing the Dynamic Chemical Environment in Graphene Liquid Cell Electron Microscopy. *J. Am. Chem. Soc.* **2019**, *141*, 4428–4437.
- (13) Crook, M. F.; Laube, C.; Moreno-Hernandez, I. A.; Kahnt, A.; Zahn, S.; Ondry, J. C.; Liu, A.; Alivisatos, A. P. Elucidating the Role of Halides and Iron during Radiolysis-Driven Oxidative Etching of Gold Nanocrystals Using Liquid Cell Transmission Electron Microscopy and Pulse Radiolysis. *J. Am. Chem. Soc.* **2021**, *143*, 11703–11713.
- (14) Hauwiller, M. R.; Ye, X.; Jones, M. R.; Chan, C. M.; Calvin, J. J.; Crook, M. F.; Zheng, H.; Alivisatos, A. P. Tracking the Effects of Ligands on Oxidative Etching of Gold Nanorods in Graphene Liquid Cell Electron Microscopy. *ACS Nano* **2020**, *14*, 10239–10250.
- (15) Dissanayake, T. U.; Wang, M.; Woehl, T. J. Revealing Reactions between the Electron Beam and Nanoparticle Capping Ligands with Correlative Fluorescence and Liquid-Phase Electron Microscopy. *ACS Appl. Mater. Interfaces* **2021**, *13*, 37553–37562.

- (16) He, K.; Sawczyk, M.; Liu, C.; Yuan, Y.; Song, B.; Deivanayagam, R.; Nie, A.; Hu, X.; Dravid, V. P.; Lu, J.; Sukotjo, C.; Lu, Y.-P.; Král, P.; Shokuhfar, T.; Shahbazian-Yassar, R. Revealing Nanoscale Mineralization Pathways of Hydroxyapatite Using in Situ Liquid Cell Transmission Electron Microscopy. *Sci. Adv.* **2020**, *6*, No. eaaz7524.
- (17) Ophus, C. Four-Dimensional Scanning Transmission Electron Microscopy (4D-STEM): From Scanning Nanodiffraction to Ptychography and Beyond. *Microsc. Microanal.* **2019**, *25*, 563–582.
- (18) Yang, Y.; Shao, Y. T.; Lu, X.; Yang, Y.; Ko, H. Y.; Distasio, R. A.; Disalvo, F. J.; Muller, D. A.; Abruña, H. D. Elucidating Cathodic Corrosion Mechanisms with Operando Electrochemical Transmission Electron Microscopy. *J. Am. Chem. Soc.* **2022**, *144*, 15698–15708.
- (19) Khelifa, A.; Byun, C.; Nelayah, J.; Wang, G.; Ricolleau, C.; Alloyeau, D. Structural Analysis of Single Nanoparticles in Liquid by Low-Dose STEM Nanodiffraction. *Micron* **2019**, *116*, 30–35.
- (20) Yuk, J. M.; Park, J.; Ercius, P.; Kim, K.; Hellebusch, D. J.; Crommie, M. F.; Lee, J. Y.; Zettl, A.; Alivisatos, A. P. High-Resolution EM of Colloidal Nanocrystal Growth Using Graphene Liquid Cells. *Science* **2012**, *336*, 61–64.
- (21) Ye, X.; Jones, M. R.; Frechette, L. B.; Chen, Q.; Powers, A. S.; Ercius, P.; Dunn, G.; Rotskoff, G. M.; Nguyen, S. C.; Adiga, V. P.; Zettl, A.; Rabani, E.; Geissler, P. L.; Alivisatos, A. P. Single-Particle Mapping of Nonequilibrium Nanocrystal Transformations. *Science* **2016**, *354*, 874–877.
- (22) Yao, L.; Ou, Z.; Luo, B.; Xu, C.; Chen, Q. Machine Learning to Reveal Nanoparticle Dynamics from Liquid-Phase TEM Videos. *ACS Cent. Sci.* **2020**, *6*, 1421–1430.
- (23) Schneider, N. M.; Norton, M. M.; Mendel, B. J.; Grogan, J. M.; Ross, F. M.; Bau, H. H. Electron-Water Interactions and Implications for Liquid Cell Electron Microscopy. *J. Phys. Chem. C* **2014**, *118*, 22373–22382.
- (24) Moreno-Hernandez, I. A.; Crook, M. F.; Ondry, J. C.; Alivisatos, A. P. Redox Mediated Control of Electrochemical Potential in Liquid Cell Electron Microscopy. *J. Am. Chem. Soc.* **2021**, *143*, 12082–12089.
- (25) Kim, K. H.; Xing, H.; Zuo, J. M.; Zhang, P.; Wang, H. TEM Based High Resolution and Low-Dose Scanning Electron Nanodiffraction Technique for Nanostructure Imaging and Analysis. *Micron* **2015**, *71*, 39–45.
- (26) Ophus, C.; Ciston, J.; Pierce, J.; Harvey, T. R.; Chess, J.; McMorran, B. J.; Czarnik, C.; Rose, H. H.; Ercius, P. Efficient Linear Phase Contrast in Scanning Transmission Electron Microscopy with Matched Illumination and Detector Interferometry. *Nat. Commun.* **2016**, *7*, 10719.
- (27) Chen, L.; Leonardi, A.; Chen, J.; Cao, M.; Li, N.; Su, D.; Zhang, Q.; Engel, M.; Ye, X. Imaging the Kinetics of Anisotropic Dissolution of Bimetallic Core–Shell Nanocubes Using Graphene Liquid Cells. *Nat. Commun.* **2020**, *11*, 3041.
- (28) Yan, C.; Byrne, D.; Ondry, J. C.; Kahnt, A.; Moreno-Hernandez, I. A.; Kamat, G. A.; Liu, Z.-J.; Laube, C.; Crook, M. F.; Zhang, Y.; Ercius, P.; Alivisatos, A. P. Facet-Selective Etching Trajectories of Individual Semiconductor Nanocrystals. *Sci. Adv.* **2022**, *8*, No. eabq1700.
- (29) Navrotsky, A.; Mazeina, L.; Majzlan, J. Size-Driven Structural and Thermodynamic Complexity in Iron Oxides. *Science* **2008**, *319*, 1635–1638.
- (30) Michel, F. M.; Ehm, L.; Antao, S. M.; Lee, P. L.; Chupas, P. J.; Liu, G.; Strongin, D. R.; Schoonen, M. A. A.; Phillips, B. L.; Parise, J. B. The Structure of Ferrihydrite, a Nanocrystalline Material. *Science* **2007**, *316*, 1726–1729.
- (31) Narayanan, S.; Firlar, E.; Rasul, M. G.; Foroozan, T.; Farajpour, N.; Covnot, L.; Shahbazian-Yassar, R.; Shokuhfar, T. On the Structure and Chemistry of Iron Oxide Cores in Human Heart and Human Spleen Ferritins Using Graphene Liquid Cell Electron Microscopy. *Nanoscale* **2019**, *11*, 16868–16878.
- (32) Wang, W.; Xu, T.; Chen, J.; Shangquan, J.; Dong, H.; Ma, H.; Zhang, Q.; Yang, J.; Bai, T.; Guo, Z.; Fang, H.; Zheng, H.; Sun, L. Solid–Liquid–Gas Reaction Accelerated by Gas Molecule Tunneling-like Effect. *Nat. Mater.* **2022**, *21*, 859–863.
- (33) Woehl, T. J.; Abellan, P. Defining the Radiation Chemistry during Liquid Cell Electron Microscopy to Enable Visualization of Nanomaterial Growth and Degradation Dynamics. *J. Microsc.* **2017**, *265*, 135–147.
- (34) Crook, M. F.; Moreno-Hernandez, I. A.; Ondry, J. C.; Ciston, J.; Bustillo, K. C.; Vargas, A.; Alivisatos, A. P. EELS Studies of Cerium Electrolyte Reveal Substantial Solute Concentration Effects in Graphene Liquid Cells. *J. Am. Chem. Soc.* **2023**, *145*, 6648–6657.
- (35) Tate, M. W.; Purohit, P.; Chamberlain, D.; Nguyen, K. X.; Hovden, R.; Chang, C. S.; Deb, P.; Turgut, E.; Heron, J. T.; Schlom, D. G.; Ralph, D. C.; Fuchs, G. D.; Shanks, K. S.; Philipp, H. T.; Muller, D. A.; Gruner, S. M. High Dynamic Range Pixel Array Detector for Scanning Transmission Electron Microscopy. *Microsc. Microanal.* **2016**, *22* (1), 237–249.
- (36) Clark, N.; Kelly, D. J.; Zhou, M.; Zou, Y. C.; Myung, C. W.; Hopkinson, D. G.; Schran, C.; Michaelides, A.; Gorbachev, R.; Haigh, S. J. Tracking Single Adatoms in Liquid in a Transmission Electron Microscope. *Nature* **2022**, *609*, 942–947.
- (37) Ni, H.-C.; Yuan, R.; Zhang, J.; Zuo, J.-M. Framework of Compressive Sensing and Data Compression for 4D-STEM. *Ultramicroscopy* **2024**, *259*, 113938.